

Detection of Potential Transit Signals in the First Twelve Quarters of *Kepler* Mission Data

Peter Tenenbaum, Jon M. Jenkins, Shawn Seader, Christopher J. Burke, Jessie L. Christiansen, Jason F. Rowe, Douglas A. Caldwell, Bruce D. Clarke, Jie Li, Elisa V. Quintana, Jeffrey C. Smith, Susan E. Thompson, and Joseph D. Twicken

SETI Institute/NASA Ames Research Center, Moffett Field, CA 94305, USA

`peter.tenenbaum@nasa.gov`

William J. Borucki, Natalie M. Batalha, Miles T. Cote, Michael R. Haas, and Dwight T. Sanderfer

NASA Ames Research Center, Moffett Field, CA 94305, USA

Forrest R. Girouard, Jennifer R. Hall, Khadeejah Ibrahim, Todd C. Klaus, Sean D. McCauliff, Christopher K. Middour, Anima Sabale, Akm Kamal Uddin, and Bill Wohler

Orbital Sciences Corporation/NASA Ames Research Center, Moffett Field, CA 94305, USA

and

Thomas Barclay and Martin Still

BAER Institute/NASA Ames Research Center, Moffett Field, CA 94305, USA

ABSTRACT

We present the results of a search for potential transit signals in the first three years of photometry data acquired by the *Kepler* Mission. The targets of the search include 112,321 targets which were observed over the full interval and an additional 79,992 targets which were observed for a subset of the full interval. From this set of targets we find a total of 11,087 targets which contain at least one signal which meets the Kepler detection criteria: those criteria are periodicity of the signal, an acceptable signal-to-noise ratio, and three tests which reject false positives. Each target containing at least one detected signal is then searched repeatedly for additional signals, which represent multi-planet systems of transiting planets. When targets with multiple detections are considered, a total of 18,406 potential transiting planet signals are found in the *Kepler* Mission dataset. The detected signals are dominated by events with relatively low signal-to-noise

ratios and by events with relatively short periods. The distribution of estimated transit depths appears to peak in the range between 20 and 30 parts per million, with a few detections down to fewer than 10 parts per million. The detections exhibit signal-to-noise ratios from 7.1σ , which is the lower cut-off for detections, to over 10,000 σ , and periods ranging from 0.5 days, which is the shortest period searched, to 525 days, which is the upper limit of achievable periods given the length of the data set and the requirement that all detections include at least 3 transits. The detected signals are compared to a set of known transit events in the *Kepler* field of view, many of which were identified by alternative methods; the comparison shows that the current search recovery rate for targets with known transit events is 98.3%.

Subject headings: planetary systems – planets and satellites: detection

1. Introduction

We have previously reported (Tenenbaum et al. 2012) on the results of searching the first 218 days of *Kepler* Mission (Borucki et al. 2010) data for potential signals indicative of transiting planets. In the intervening time, there have been two developments in the search for potential exoplanets in the *Kepler* dataset. First, the algorithms used in the *Kepler* analysis pipeline have undergone dramatic improvements. Second, the data available for searching has expanded from 218 days to 1050.5 days. This massive increase in data volume makes possible searches for exoplanets with much longer orbital periods, as well as searches for extremely small exoplanets with relatively short period orbits. In this study we report on the results of searching the current set of *Kepler* observations with the upgraded analysis pipeline. This study can be considered as an update of the previous report (Tenenbaum et al. 2012).

1.1. *Kepler* Science Data

The operational parameters of the *Kepler* Mission have been extensively reported (Haas et al. 2010). In brief: the *Kepler* spacecraft is in an Earth-trailing heliocentric orbit of 372 day period. Its single instrument, the *Kepler* photometer, points almost constantly at a 115 square degree region of the sky centered on $\alpha = 19^{\text{h}}22^{\text{m}}40^{\text{s}}$, $\delta = +44.5^\circ$. During science operations, photometric data is taken in 29.4 minute integrations, known within *Kepler* as “long cadences” (as distinguished from “short cadences,” which are 1/30 of a “long cadence”

and are collected for a small subset of targets). In order to maintain the correct orientation of the solar panels and thermal radiator, the spacecraft rotates about the photometer boresight axis by 90° approximately every 93 days, the interval at a given orientation being referred to as a “quarter.” A consequence of this rotation is that each target star is observed each year on 4 different readout channels on the focal plane. Science acquisition is interrupted for monthly downlinking of pixel data, maneuvering from one quarter’s attitude to the next, reaction wheel desaturation (one 29.4 minute sample is lost for this purpose approximately every 3 days), and a variety of spacecraft anomalies.

The data acquisition period for this analysis begins at 2009 May 12 00:00:00 UTC, ends at 2012 March 28 12:47:26 UTC, and contains 51,412 sample intervals of 29.4 minutes. Of these, 47,588 intervals are dedicated to science data acquisition, the balance of 3,824 intervals being consumed by the interruptions listed above. During this period the spacecraft performed 11 axial rotations, resulting in 12 quarters worth of data.

A total of 192,313 targets were observed by *Kepler* during the 12 quarters of data acquisition, and were subsequently searched for indications of transiting planets. Of those, 112,321 were observed in all 12 quarters; the balance of 79,992 were observed only in a subset of quarters. Figure 1 shows the distribution of targets according to the number of quarters observed. Observation of a target in a subset of quarters can occur for any of three reasons. The most significant cause of limited observation is an onboard electronics failure which occurred on 2010 January 23, one month into quarter 4: this failure resulted in the subsequent loss of all data from 4 of the 84 CCD readouts on the focal plane (specifically, the 4 CCD readouts in Module 3). Due to the quarterly rotation of the spacecraft, this failure produced a “blind spot” in the *Kepler* field of view which moves relative to the target stars, causing a large number of targets to be visible only 75% of the time. Any target which falls onto Module 3 was only observed in 10 out of 12 quarters. The 28,965 stars which were observed for 10 quarters as shown in Figure 1 are mainly due to this effect. A second limitation on the number of quarters for which a target is observed is that the process of target selection and prioritization has evolved over the life of the *Kepler* Mission; targets which are added or removed subsequent to Quarter 1 will not be observed during all quarters. Additionally, a fraction of *Kepler*’s observing capacity is reserved for use by the *Kepler* Guest Observer (GO) and Asteroseismic Science Consortium (KASC) programs; the targets observed in these programs are frequently updated, resulting in a number of targets observed for relatively short intervals. Finally, due to small asymmetries in the construction of the focal plane, a small number of targets cannot be observed in all spacecraft orientations: in some quarters these targets are imaged onto one or another CCD detector, while in some quarters the target images fall between the detectors. In total, 28,826 targets were observed in 8 or fewer quarters; 43,339 targets were observed for 9 or 10 quarters; and 7,819 targets

were observed for 11 quarters.

In addition to the aforementioned 192,313 targets which were searched for planets, a total of 2,123 known eclipsing binaries which were observed but not searched for transiting planet signatures. This was done for operational reasons. The *Kepler* processing pipeline has limited capacity to identify circumbinary planets because their transit signatures are generally neither periodic nor of constant duration. However, the eclipses of an eclipsing binary system mimic planetary transits with sufficient fidelity to be identified by TPS as potential signals of transiting planets. These known eclipsing binaries were removed to reduce the computational and human burden which would otherwise have been imposed by their false-positive detections.

1.2. Pre-Search Processing

The processing of pixel data from the *Kepler* spacecraft, prior to the search for transiting planet signatures, is summarized elsewhere (Jenkins et al. 2010a). The processing step which has seen the most dramatic change is Pre-Search Data Conditioning (PDC). The purpose of PDC is to remove variations in the flux time series which are generated by changes in the spacecraft environment or other systematic effects. The original PDC algorithm determined the systematics by performing a robust least-squares fit of assorted spacecraft engineering variables to each flux time series, and then subtracting the systematics thus determined to yield a conditioned flux time series (Twicken et al. 2010b). While such an approach is guaranteed to reduce the bulk RMS variation of each target’s flux, it can also distort the true stellar variations and can even add variability on timescales of interest for planet searches. Both of these unwanted side effects are driven by the same source: the least-squares fit is removing variability which is *coincidentally* correlated with some engineering variable, but not *causally* related.

This unwanted behavior is corrected by applying a Bayesian approach to constrain the fitted amplitudes of systematic error terms which are then removed from the light curves. This process allows the algorithm to deduce “reasonable” values for the correlation of each identified systematic to the light curves, and thus to reject correlations which are wildly out of family. Additionally, the ensemble of target star data across a large number of stars is used to empirically identify systematic trends in the light curves, rather than relying upon the available spacecraft engineering data. The algorithm is fully described elsewhere (Smith et al. 2012; Stumpe et al. 2012).

In addition to the corrections described above, the current PDC algorithm identifies and

corrects the signature of a cosmic ray related artifact known as a Sudden Pixel Sensitivity Dropout (SPSD). An PSD occurs when a cosmic ray produces a step reduction in the quantum efficiency of a pixel; the reduction is typically of order one percent, and the quantum efficiency partially recovers, typically over a period of hours to days. Because an PSD bears a superficial resemblance to a transit signature (at least to a computer), efficient removal of PSDs without inadvertent removal of actual transits is a crucial step in data conditioning for *Kepler*. Unlike environmental signatures, PSDs are completely uncorrelated from one target star to another, and thus are removed from the data via a separate algorithm within PDC.

2. Transiting Planet Search

The Transiting Planet Search (TPS) algorithm is described in some detail in Jenkins (2002) and Jenkins et al. (2010b), as well as Tenenbaum et al. (2012). The improvements in the algorithm since Tenenbaum et al. (2012) are summarized below.

2.1. Edge Detrending of Contiguous Blocks of Flight Data

The algorithm which was previously used to remove trends at the ends of single-quarter data segments was replaced with an algorithm which performs a robust fit of the form:

$$y = P_1 \exp(-x/P_2) + P_3x + P_4 + P_5 \exp[(x - 1)/P_6], \quad (1)$$

where y is the median-corrected flux, x is the sample time normalized to a range from 0 to 1, and P_1 through P_6 are the parameters of the fit. In words, Equation 1 fits a line plus two exponential edge trends, one at the leading edge of the data region and one at the trailing region, with both the amplitude and the time constant of the exponentials as fit parameters. The form in Equation 1 was found to match the actual edge trends as well as the constrained polynomial fit which had previously been used. The advantages of the reformulated edge-trend removal are: a reduced number of assumptions and/or configuration parameters for the fit; use of the full data segment for the entire fit; robust fitting; and the fact that the new fit does not under any circumstances introduce a polynomial “wave” into the data segment in an attempt to correct the edges (i.e., over fitting). Additionally, whereas in the past the edge detrending was applied only to full quarters of data, in the current implementation it is applied at any time when there was an interruption of data acquisition to change the spacecraft orientation. This was done to mitigate the thermal transients which occur when the spacecraft attitude is changed. Attitude change incidents include all data downlink

intervals, plus any transitions into or out of safe mode.

2.2. Detection and Vetoing of Potential Signals

The first step in detection of potential signals is described in Section 2 of Tenenbaum et al. (2012): a wavelet-based, adaptive matched filter is utilized to search for periodic reductions in flux occurring against the non-white, non-stationary background of stellar variability. The significance of such a reduction is known as its Multiple Event Statistic. The Multiple Event Statistic is computed across a two-dimensional grid of signal period and epoch of first transit, and across 14 trial transit pulse durations; the maximum Multiple Event Statistic from this set is captured, along with the combination of period, epoch, and transit pulse duration (henceforth "signal timing") which generated it; target stars for which the maximum Multiple Event Statistic falls below the specified detection threshold of 7.1σ are rejected from further analysis. The requirement that the maximum Multiple Event Statistic exceed 7.1σ removes from further consideration 76,668 targets, leaving 115,645 with at least one potential transit signal which lies above this threshold.

The principal weakness of the Multiple Event Statistic calculation is that it cannot discriminate between a true train of transit events (which have uniform depth, duration, and shape to within the precision limits of the instrument) and a chance combination of dissimilar events which coincidentally occur within a flux time series. As an example, consider a flux time series for which the combined differential photometric precision (CDPP) for transit detection is 50 parts per million (PPM) at all times (Christiansen et al. 2012). If the flux time series contains 4 uniformly-spaced transits of with uniform depths 250 PPM, the resulting Multiple Event Statistic for that period and epoch will be 10σ , and will be reported as an above-threshold event by the Multiple Event Statistic calculation. On the other hand, if the 4 transits are uniformly spaced but do not have uniform depth – for example, if the depths of the 4 transits are 20 PPM, 30 PPM, 50 PPM, and 900 PPM, respectively – the Multiple Event Statistic for this combination of events will also be 10σ , and will also be reported as an above-threshold event by the Multiple Event Statistic calculation. While the former scenario might be the signature of a transiting planet, the latter clearly is not. Thus, a Multiple Event Statistic which is above the detection threshold is a necessary but not sufficient condition for identifying a potential transiting planet signature. More generally, while the matched filter approach is optimal with respect to rejecting the null hypothesis, it is insufficient for discrimination between competing alternate models. For this reason, once a Multiple Event Statistic above the detection threshold is identified, event thus detected is subjected to a series of tests which are designed to discriminate between potential transit signatures and

heterogeneous combinations of unrelated events. These tests accept the former while vetoing the latter.

2.2.1. *Robust Statistic Veto of False Positive Detections*

In the first test used for vetoing false positives, a model light curve consisting of a train of model transit pulses is directly fitted to the flux time series. The model transit pulses are square waves, with their period, epoch, and duration determined by the signal timing produced in the Multiple Event Statistic test. In order to eliminate the effect of stellar variations, both the flux time series and the model transit pulse train are whitened, as described in Jenkins et al. (2010b). The fit is performed robustly, in order to reduce the influence of impulsive outliers in the flux time series; the Robust Statistic, which is the signal-to-noise ratio estimated from the fit, is then used to reject false positives. Specifically, a large value of the Robust Statistic indicates a detection in which the transits are reasonably uniform in depth and duration, which is characteristic of true transit signatures; a small value indicates that the Multiple Event Statistic has been formed from a combination of heterogeneous transit-like events with unequal depths, which is characteristic of false positives. A threshold of 6.4σ for the Robust Statistic rejects 79,030 targets, leaving 36,614 targets which require further scrutiny.

2.2.2. χ^2 Veto of False Positive Detections

In the second test used for vetoing of false positives, we take advantage of the fact that, given the signal timing and the magnitude of the Multiple Event Statistic, the expected frequency-domain content of the transits can also be calculated and compared to the frequency-domain content of the signal identified by the Multiple Event Statistic test. As shown briefly in Appendix A, and more thoroughly in Seader et al. (2012), knowledge of the expected frequency-domain distribution of each transit allows construction of two functions, each of which is expected to be distributed according to a χ^2 distribution. These functions are then combined with the Multiple Event Statistic of the potential signal, as shown in Appendix A. By requiring that the values of the two resulting discriminators, $X_{(1)}$ and $X_{(2)}$, both exceed 7.0, we veto an additional 25,506 targets, yielding 11,108 targets which contain potential transiting planet signatures. An event which has passed all four tests – Multiple Event Statistic, Robust Statistic, and χ^2 discriminators – is referred to as a Threshold Crossing Event (TCE).

2.3. Iterative Rejection of False Positives and Re-Searching of the Flux Time Series

Prior versions of TPS suffered from a significant design weakness: in cases in which the strongest transit-like feature was vetoed, the search of that target would terminate. In this way a strong but low-quality transit-like signal could inadvertently mask a weaker but higher-quality event. This flaw is addressed in the current version of TPS: in the event that an apparent transit is vetoed, TPS goes on to search for additional transit signatures in the same light curve. Because the search of additional periods and epochs can potentially be extremely time-consuming, for operational purposes it is necessary to limit the number of iterations of searching which are permitted for a given target and a given trial transit pulse duration. At present the limit is set to 1000 iterations of re-searching. In the analysis reported here, approximately three quarters of all TCEs occurred on the first iteration of the search, with the balance TCEs detected on subsequent iterations. The largest number of iterations required to detect a TCE was 404.

2.4. Removal of Non-Periodic Transit-Like Features

The benefits of the multiple iterations of search, described above, can only be fully exploited in the absence of relatively strong non-astrophysical single events. Such strong events will cause the Multiple Event Statistic to exceed the 7.1σ threshold for large numbers of possible periods: folding a single strong event with a small number of weak events will produce a large Multiple Event Statistic, and there are an extremely large number of period-epoch combinations which will result in such a folding. If this happens, the 1000 iterations of searching can easily be exhausted in the process of eliminating a fraction of the spurious Multiple Event Statistics caused by a single strong event. Such an outcome can be avoided if these strong events are identified and removed prior to folding, but such removals are obviously dangerous: without prior knowledge, a feature in the data which is identified as a non-astrophysical event, and removed, could actually be a strong transit. For this reason, any event removal must be used sparingly. TPS addresses this issue in two ways. First, a minimum number of transits is required for an event to be accepted, since the probability of such chance combinations yielding a Multiple Event Statistic over threshold decreases as the number of events folded together increases. At present, the threshold number of transits is 3. Second, the current version of TPS is permitted to remove one, and only one, single event, and only in the case in which the first iteration of planet searching produces a strongest event which exceeds the Multiple Event Statistic threshold of 7.1σ but which is then vetoed by RS, $X_{(1)}$, or $X_{(2)}$. In such a case the strongest single event in the time series is removed,

if and only if the strongest single event has an amplitude which is greater than the Multiple Event Statistic threshold multiplied by the square root of the minimum number of transits ($7.1 \sigma \times \sqrt{3}$, or 12.3σ for the current parameter choices). Out of the 11,108 TCEs, 2,193 are found on light curves which have had such a feature removed. Additionally, on each target the number of such identifiable features is counted and recorded, regardless of whether any such events are removed. Out of all 192,313 targets, the number which have at least one identifiable strong single event is 46,481. Figure 2 shows the distribution of the number of strong events for targets which have at least one such event. Note that the distribution is strongly peaked towards small numbers of events, implying that it is worth considering the option of using more aggressive removal of features in future TPS runs.

2.5. Limitation on Allowable Transit Duty Cycles

During development of the most recent version of TPS, it was observed that a substantial number of false positives were produced with a short period and a long trial transit pulse duration. In the processing run reported on here, we limit the ratio of the trial transit pulse duration to the detected period of the signal to be less than 0.16 in order to mitigate this category of false positive detections. By comparison, the transit duration to transit period ratio for a central transit of the Earth is approximately 7.4×10^{-4} .

2.6. Detection of Multiple Planet Systems

In Wu et al. (2010), the process for detection of multiple planet systems is described. In brief, for each target star which yields a valid detection as described above, a planet model is fit to the flux time series, using the period and epoch of the TCE as a starting point for the fit; the transit signatures from the fitted planet model are removed from the flux time series; and the residual flux time series is then searched for additional TCEs. The subsequent TCE search is performed using the same TPS algorithm as is used for the initial search. When multiple planet detections are included, the total number of TCEs increases to 18,427.

Following the detection and model fitting described above, an additional set of automated analyses are performed which allow astrophysical false positives, such as background eclipsing binaries, to be ruled out. For the purposes of the discussion below, we will consider only the TCEs for which the additional automated analyses were successfully completed: this set includes 18,406 TCEs falling on 11,087 targets. Of the 21 excluded targets, 19 non-stellar “super-aperture” targets, for which the automated post-detection analyses cannot be

performed, while 2 are conventional *Kepler* targets for which the automated post-detection analyses failed due to software errors. Each of the excluded targets produced a single TCE.

3. Detected Signals of Potential Transiting Planets

Figure 3 shows the epoch and period of the 18,406 detections, with period in days and epoch in Kepler-Modified Julian Date (KJD), which is Julian Date - 2,454,833.0. While Figure 3 is relatively free of obvious artifacts, there is an evident overabundance of detections at periods of approximately one year. Figure 4 shows the distribution of periods from Figure 3; the overabundance is even clearer here, with 2,042 TCEs with periods between 300 and 400 days as compared to 305 TCEs with periods of 200 to 300 days and 168 TCEs with periods of 400 to 500 days.

Figure 5 shows the participation of the various detector channels on the *Kepler* focal plane in TCEs with periods between 300 and 400 days: each sub-image shows one quarter, and the relative intensity of each channel represents the participation, of that channel in that quarter, in the 2,042 TCEs. A small number of channels are disproportionately involved in these TCEs, mainly channels which are known to suffer from excess noise due to issues in the readout electronics (Gilliland et al. 2011; Caldwell et al. 2012). As *Kepler* rotates each quarter, certain stars will typically be imaged onto one of these misbehaving channels once per year; this will result in detections on those stars with periods of approximately 1 year. Efforts to manage the excess noise of these channels in *Kepler* data processing are ongoing.

Figure 6 shows the distribution of detections in the plane of orbital period and Multiple Event Statistic. Note that the overabundance of detections at one year is completely dominated by relatively weak signals. Figure 7 shows the distribution of Multiple Event Statistics: on the left is the distribution of 17,547 detections with Multiple Event Statistic less than or equal to 100σ ; the right panel shows the same but for the 15,007 detections with Multiple Event Statistic less than or equal to 20σ . Figure 8 shows the distribution of detected periods: on the left is the 5,043 detections with periods over 15 days, on the right is the 13,363 detections with periods less than 15 days. As compared to Figure 6 in Tenenbaum et al. (2012), the right side of Figure 8 is far more strongly peaked towards short periods. Note that, in addition to the excess of detections with periods close to 1 year, there is a smaller excess of detections with periods of 0.5 years. This peak is caused by the presence of two high-noise channels which are located symmetrically opposite one another on the focal plane, specifically Module 17, Output 2, and Module 9, Output 2: stars which are imaged onto one of these channels will be imaged onto the other 6 months later.

Figure 9 shows the distribution in estimated transit depths. These depths are estimated from the event statistics and the noise properties of each light curve, as described in Tenenbaum et al. (2012). The top plot shows the 16,095 signals which have estimated depths of 1,000 parts per million (PPM) or less; the bottom plot shows the 8,060 cases with estimated depths of 100 PPM or less. These sub-distributions contain 87.4% and 43.8%, respectively, of all the detections in this dataset. Comparing to the same transit depth ranges in Tenenbaum et al. (2012), we find that in the processing of the first 3 quarters of data the totals were 72.3% and 13.2%, respectively. This increased sensitivity to weaker transits is driven in the main by the vastly increased amount of data collected since the end of Quarter 3.

Figure 10 shows the distribution of transit duty cycles for all detections, where the transit duty cycle is defined to be the ratio of the trial transit pulse duration to the detected period of the transit (effectively, the fraction of the time during which the TCE is in transit). The top plot shows all 18,406 TCEs, while the bottom plot shows the 7,721 TCEs with transit duty cycle below 0.04. Figure 11 shows the relationship between period and transit duty cycle for all 18,406 detections. As expected, the relationship is quantized due to the quantization of trial transit pulse durations utilized in the TPS detection algorithm, and as a consequence of this quantization the period and transit duty cycle are inversely proportional for a given trial transit pulse duration. Figure 11 also demonstrates why there is an abundance of events with transit duty cycles of approximately 0.002 shown in Figure 10: this is actually a reflection of the abundance of events with periods near 1 year, for which the possible transit duty cycles are all in the realm of 1×10^{-4} to 0.002.

Detailed information on all TCEs which contributed to this analysis can be found at the NASA Exoplanet Archive: <http://exoplanetarchive.ipac.caltech.edu/>.

3.1. Comparison with Known Kepler Objects of Interest (KOIs)

In order to gauge the performance of TPS as a detector of periodic transit-like phenomena, it is necessary to compare the set of TCEs to a set of known events which can function as a “ground truth”. For this purpose, we use the list of Kepler Objects of Interest (KOIs). Out of the current set of KOIs (Burke, C.J. et al. 2012, in preparation), we have selected 2,630 KOIs which are judged reasonable for comparison to the TCE list: these are KOIs for which the signal to noise ratio is high enough to permit detection in TPS, the number of transits which fall within the 12 quarters of *Kepler* data is 3 or more, and which do not fall on targets which were excluded from TPS processing. The selected set of KOIs includes planet candidates, known astrophysical false positives (mainly eclipsing binaries and background

eclipsing binaries), and objects which have not yet been characterized as planetary or non-planetary; for the purpose of the comparison, it is sufficient that each KOI be reasonably expected to produce a TCE.

The comparison of the KOI and TCE lists is complicated by the fact that any target star can have multiple KOIs and/or multiple TCEs, and the multiplicities of the two are obviously not guaranteed to agree. As a first step, we compared the number of TCEs on each KOI target star with the number of KOIs on those stars. The result of this comparison is as follows:

- A total of 31 KOIs do not have a corresponding TCE
- The remaining 2,599 KOIs were matched one-for-one by TCEs which occurred on the same target stars
- 337 KOI target stars produced more TCEs than their known KOIs, resulting in a total of 438 TCEs which fall on KOI targets but are not matched by known KOIs.

3.1.1. Failure to Detect Short-period KOIs due to Data Artifacts

Subsequent analysis of the KOIs which were not matched by TCEs showed that 21 out of the 31 had relatively short periods, typically under 2 weeks. Figure 12 shows the maximum Multiple Event Statistic as a function of period for a selected target in this group. The period and Multiple Event Statistic of the KOI on this target star is indicated with a marker in the plot. As shown in Figure 12, the Multiple Event Statistic is dramatically and systematically larger for long periods than for short periods, with a gross pattern of the Multiple Event Statistic rising as the square root of the period.

The root cause of this pattern is a small number of strong transit-like data anomalies which are randomly distributed amongst the flux time series. During the folding process which results in Figure 12, the anomalies are combined with background noise to produce strong Multiple Event Statistics. For short periods, the number of events folded together is large, thus there are many background noise events combined with a single data anomaly; as a result, the Multiple Event statistic is relatively small due to the dilution from the many background noise events. For long periods, because the number of noise events is small, the data anomaly is relatively undiluted and the resulting Multiple Event Statistic is relatively large.

A Multiple Event Statistic which is composed of one strong transit-like anomaly and multiple non-transit-like background noise signals will not survive the Robust Statistic and

chi-square vetoes, as it does not match the quantitative signatures of a true transit pulse train which those vetoes require. Unfortunately, as noted above, the ability of TPS to reject large numbers of such false detections in a single light curve has been limited for reasons of computational performance: the 1,000 combinations of period and transit epoch which produce the strongest Multiple Event Statistics are searched, after which the search algorithm declares that no transit signatures were found. In the case of a target such as the one selected for Figure 12, the 1,000 strongest signals are all at the long-period end of the distribution, and the search iterations are exhausted before the actual signal at 3.766 days is examined.

In the limit where strong transit-like data anomalies are distributed uniformly and randomly throughout the dataset, there will inevitably be some targets for which early quarters of data contain no anomalies but later quarters contain one or more. If such a target also contains a short-period, low-intensity transit signature, then the transit signature will be detectable only so long as the data used for the detection was entirely acquired prior to the first anomaly occurrence. This appears to be the case for the 21 instances of short-period, low-intensity KOIs which were not detected by the most recent TPS run. Note that this is one of those unusual situations in which a 12 quarter dataset does not permit detection of a signal which was apparent in a 3- or 6-quarter dataset.

3.1.2. Matching of KOI and TCE Ephemerides

Detection of a TCE on a KOI target is a necessary but not sufficient condition to determine that the TCE is a detection of the KOI. An additional requirement is that the TCE and KOI are referring to the same transit signature. This is typically best determined by matching the ephemerides of the two signatures. For this purpose we use an ephemeris-matching calculation described in Appendix B. The resulting match parameter varies from a value of zero, indicating no match whatsoever, to a value of one, indicating a perfect match within the limits of the *Kepler* data and data processing algorithm. In the case of a target star which has multiple KOIs and/or multiple TCEs, it is necessary to attempt to correctly match each KOI with the corresponding TCE. A subtlety in this process is that it is at least conceivable that multiple KOIs will be best matched by the same TCE. For example, consider a target which has two KOIs, with periods of 0.5 and 1.0 years, and three TCEs, with periods of 0.5, 0.1, and 0.03144 years. Depending on the detailed transit timings, it is at least conceivable that the TCE with the 0.5 year period will be the best match out of the 3 TCEs for both the 0.5 year and 1.0 year period KOIs. In order to ensure that each TCE is paired with one and only one KOI, the following approach is used:

- Compute the ephemeris matches for all $n_{\text{KOI}} \times n_{\text{TCE}}$ possible matches between KOI and TCE
- Find the best match in that matrix, and pair the corresponding KOI and TCE with one another
- Eliminate both the KOI and the TCE which have now been paired
- Repeat the exercise with the remaining $(n_{\text{KOI}} - 1) \times (n_{\text{TCE}} - 1)$ possible matches, and iterate until either the number of TCEs or the number of KOIs on the given target star are exhausted.

Figure 13 shows the value of the ephemeris match between each of the 2,599 KOIs and the TCE on that star which provided the closest match. The values in Figure 13 are sorted into descending order. Of the 2,599 match values, only 104 are less than 1.0, with 2,495 identically equal to 1. Of these 104 cases, 91 are either harmonic mismatches between the TCE and the KOI (especially in cases where the KOI period is under the 0.5 day minimum period used in TPS) or cases in which the KOI timing was determined using only data from early quarters, resulting in errors when extrapolating the timing to the full 12 quarters used in this analysis. The remaining classes of discrepancy between TCE and KOI are as follows:

- In 8 cases, transit timing variations (TTV) cause confusion for TPS, which is explicitly designed to find periodic transit signatures; this generally results in a tremendous period mismatch between the KOI timing and the TCE, since TPS will usually detect a tiny subset of all transits.
- In 3 cases, the KOI and the TCE have inconsistent transit timing signatures, but both signatures appear valid. In each of these cases it is assumed that TPS has identified a heretofore-unknown transit signature on the KOI target, but then failed to detect the known KOI during the multiple-planet search which followed detection of the new TCE. For this reason, these cases are classified as failures of the TPS algorithm to recover the known KOIs.
- In 2 cases the KOI timing clearly produces a transit signature and the TCE timing clearly does not.

3.1.3. Conclusion of TCE-KOI Comparison

Out of 2,630 KOIs which could be expected to produce TCEs, 44 did not produce TCEs. This includes 31 cases in which there was no TCE and 13 cases in which a TCE was

produced but the timing of the TCE did not match the timing of the KOI, even when “near misses” such as harmonic or sub-harmonic detection are taken into account. This yields a KOI recovery rate of 2,586 out of 2,630, or 98.3%.

3.1.4. *Transit Duty Cycle of TCEs Matched to KOIs*

Figure 14 shows the distribution of TCE transit duty cycles for the 2,495 cases in which the TCE-KOI ephemeris match is identically equal to 1, as well as the distribution for the 2,205 cases in which the ephemeris match is identically equal to 1 and the transit duty cycle is below 0.04. When compared to Figure 10, which shows the transit duty cycle for all TCEs, two differences are instantly apparent. First, and least surprisingly, the spike in transit duty cycle values around 0.002 which is visible in Figure 10 is absent from Figure 14. This is because the spike in the former is due to the spurious, anomaly-driven detections at 1 year period which are caused by CCD readouts with unusually strong noise properties; these spurious detections are not present in the set of KOIs, thanks to the greater degree of scrutiny on KOIs which allows elimination of such false detections. Second, the KOI transit duty cycle distribution shows a monotonic reduction in the number of KOIs as the transit duty cycle is increased; the TCE distribution shows a reduction from 0.01 to 0.04 transit duty cycle, and an increase from 0.04 to 0.16. Quantitatively, while 58% of all TCE detections in Figure 10 have a transit duty cycle of 0.04 or greater, only 12% of all KOIs in Figure 14 have transit duty cycle above 0.04. The implication is that the long transit duty cycle TCEs are most likely dominated by false positive detections, and that further reduction in the maximum allowed transit duty cycle from the current value of 0.16 would result in further reduction of the fraction of false positive TCEs, though of course some study would be needed to determine an optimum threshold for the transit duty cycle.

4. Conclusions

The *Kepler* Transiting Planet Search (TPS) algorithm has been run on 192,313 targets in the *Kepler* field of view, including 112,321 targets which have been observed near-continuously for the first 12 quarters of the mission. Potential signals of transiting planets were detected on 11,087 of these targets. When subjected to further searches for multiple planets, the total number of detected signals grew to 18,406. Comparison with a known and vetted set of transit-like astrophysical signatures, the Kepler Objects of Interest (KOIs), demonstrates that within the parameter regime of the search algorithm and the KOIs the recovery rate of known events is 98.3%.

5. Acknowledgements

Funding for this mission is provided by NASA’s Space Mission Directorate. The contributions of Hema Chandrasekaran and Chris Henze have been essential in the studies documented here.

A. Threshold Crossing Event Vetoes using Chi-Square Discriminators

The basic idea behind the construction of the test statistic is to break up the matched filter output into several contributions and compare each contribution with what is expected. What follows in this paragraph is taken from Allen (2004) for completeness. Mathematically we have,

$$z = \sum_{j=1}^b z_j , \quad (\text{A1})$$

where the z_j are additive chunks of the filter output that when added together reproduce exactly the output value of the filter, here denoted z . Next consider the b quantities defined by

$$\Delta z_j \equiv z_j - q_j z , \quad (\text{A2})$$

where

$$\sum_{j=1}^b q_j = 1 , \quad (\text{A3})$$

and the q_j are the expected fractional contribution to z from the j ’th contribution. The Δz_j are then the set of difference between the j actual contributions and expected contributions. By definition, Δz_j ’s sum to zero

$$\sum_{j=1}^b \Delta z_j = 0 \quad (\text{A4})$$

and their expectation values vanish

$$\langle \Delta z_j \rangle = 0 . \quad (\text{A5})$$

The χ^2 statistic is then defined as

$$\chi^2 = \sum_{j=1}^b (\Delta z_j)^2 / q_j . \quad (\text{A6})$$

Note that with some basic assumptions on the detector noise (namely, that the noise after whitening is zero mean, unit variance, and uncorrelated) the expectation values of these

quantities are independent of whether or not a signal is present in the data, making this an ideal discriminator for noise events.

This concept can now be applied in various ways to the components of the single event statistics and multiple event statistics. Beginning with the single event statistic time series $z(n)$:

$$z(n) = \frac{\mathbb{N}(n)}{\sqrt{\mathbb{D}(n)}}, \quad (\text{A7})$$

where

$$\begin{aligned} \mathbb{N}(n) &\equiv \sum_{i=1}^M 2^{-\min(i, M-1)} \left\{ \left[\frac{x_i}{\hat{\sigma}_i^2} \right] * \tilde{s}_i \right\} (n) = \sum_{i=1}^M \mathbb{N}_i(n), \\ \mathbb{D}(n) &\equiv \sum_{i=1}^M 2^{-\min(i, M-1)} [\hat{\sigma}_i^{-2} * \tilde{s}_i^2] (n) = \sum_{i=1}^M \mathbb{D}_i(n), \end{aligned} \quad (\text{A8})$$

where M , x_i , $\hat{\sigma}_i$, and \tilde{s}_i are defined in Appendix A of Tenenbaum et al. (2012). Qualitatively, the time series $\mathbb{N}(n)$ represents the amplitude of a transit-like signal centered at sample n , $\mathbb{D}(n)$ represents the square of the noise limit for detecting a transit-like signature at sample n ; $z(n)$ therefore represents the significance of a transit-like signature detected at sample n . Equation A8 also defines quantities \mathbb{N}_i and \mathbb{D}_i : these are the contributions to \mathbb{N} and \mathbb{D} , respectively, from frequency band i . Choosing a particular point in transit duration, period, and epoch space, $\{D, T, t_0\}$, selects out a set of data samples $\{A\}$, one for each transit, that start with the sample corresponding to the epoch t_0 and are spaced T samples apart. These cadences form a subset of $\{n\}$, $A \subset \{1, 2, \dots, P\}$, where P is the number of transits in the dataset. The Multiple Event Statistic is then constructed as:

$$Z(D, T, t_0) = \sum_{i \in A} \mathbb{N}(i) / \sqrt{\sum_{i \in A} \mathbb{D}(i)} . \quad (\text{A9})$$

One version of the χ^2 can be constructed by focusing on the wavelet contributions to the Single Event Statistics. If we start now with (A7), we can make the identifications:

$$z_i(n) = \frac{\mathbb{N}_i(n)}{\sqrt{\mathbb{D}(n)}} \quad (\text{A10})$$

$$q_i(n) = \frac{\mathbb{D}_i(n)}{\mathbb{D}(n)}, \quad (\text{A11})$$

where now the $z_i(n)$ are the actual contributions the the SES time series from the i 'th wavelet component and $q_i(n)$ are the corresponding expected contributions. Now the χ^2 statistic can be formed:

$$\Delta z_i(n) = z_i(n) - q_i(n)z(n) \quad (\text{A12})$$

$$\chi^2(n) = \sum_{i=1}^M \frac{[\Delta z_i(n)]^2}{q_i(n)} . \quad (\text{A13})$$

Using the previously mentioned noise assumptions, this statistic should be χ^2 distributed with $M - 1$ degrees of freedom; due to leakage between the wavelet components it turns out to be gamma distributed in actual practice. We have a value for this statistic at each n , so we can form a coherent statistic by adding up the points that contribute to the Multiple Event Statistic at times j where $j \in A$. This will give us, $\chi_{(1)}^2$,

$$\begin{aligned} \chi_{(1)}^2 &= \sum_{j \in A} \chi^2(j) \\ &= \sum_{j \in A} \sum_{i=1}^M \frac{[\Delta z_i(j)]^2}{q_i(j)} \\ &= \sum_{j \in A} \sum_{i=1}^M \frac{\Delta z_{ij}^2}{q_{ij}} , \end{aligned} \quad (\text{A14})$$

where the Δz_{ij} and q_{ij} have been introduced for notational convenience. Using the previous assumptions on noise and assuming a perfect match between the signal and template, this statistic is χ^2 -distributed with $P(M - 1)$ degrees of freedom.

Another version of the χ^2 statistics can be constructed by examining the P temporal contributions to the Multiple Event Statistic. To begin, Equation A9 can be rewritten using the quantities defined for notational convenience:

$$\begin{aligned} Z &= \frac{\sum_{j \in A} \mathbb{N}(j)}{\sqrt{\sum_{j \in A} \mathbb{D}(j)}} \\ &= \frac{\sum_{j \in A} \sum_{i=1}^M \mathbb{N}_i(j)}{\sqrt{\sum_{j \in A} \sum_{i=1}^M \mathbb{D}_i(j)}} \\ &= \frac{\sum_{j \in A} \sum_{i=1}^M \mathbb{N}_{ij}}{\sqrt{\sum_{j \in A} \sum_{i=1}^M \mathbb{D}_{ij}}} . \end{aligned} \quad (\text{A15})$$

Now, choosing to examine the contributions to the Multiple Event Statistic from each $j \in A$,

$$Z_j = \frac{\sum_{i=1}^M \mathbb{N}_{ij}}{\sqrt{\sum_{k \in A} \sum_{i=1}^M \mathbb{D}_{ik}}} \quad (\text{A16})$$

$$Q_j = \frac{\sum_{i=1}^M \mathbb{D}_{ij}}{\sum_{k \in A} \sum_{i=1}^M \mathbb{D}_{ik}} , \quad (\text{A17})$$

where now Z_j are the actual temporal contributions to the Multiple Event Statistic and the Q_j are the expected contributions. Now, $\chi^2_{(2)}$ can be constructed:

$$\Delta Z_j = Z_j - Q_j Z \quad (\text{A18})$$

$$\chi^2_{(2)} = \sum_{j \in A} \frac{\Delta Z_j^2}{Q_j} . \quad (\text{A19})$$

Under the previous noise assumptions, this statistic is χ^2 -distributed with $P - 1$ degrees of freedom. Since we have summed over the wavelet contributions prior to computing this statistic it avoids the leakage issue and turns out to be a much more powerful discriminator. Note that dozens of other version of the chi-square veto have been formulated and investigated with real data, and indeed an infinity of such statistics exists. These two versions give us the greatest detection efficiency while simultaneously minimizing the false alarm rate.

The results quoted in what follows are subject to a subtle issue discovered after the Q1-Q12 run was completed. The whitening coefficients in the calculation should be robust against the presence of a signal in the data since they are computed using a moving circular median absolute deviation. However, the χ^2 statistics are very sensitive to any signal dependence of the whitening coefficients, however small it may be, due to the way in which they are constructed. The code is now being re-written so that in-transit cadences are first gapped and filled to re-compute the whitening coefficients for use in the χ^2 calculation. This should explicitly remove the signal dependence and give us more vetoing power.

Based on analysis of known true-positive and expected false-positive targets, TPS uses the following discriminators in vetoing false-positive detections:

$$\begin{aligned} X_{(1)} &\equiv \frac{Z \sqrt{P(M-1)}}{\sqrt{\chi^2_{(1)}}}, \\ X_{(2)} &\equiv \frac{Z \sqrt{P-1}}{\sqrt{\chi^2_{(2)}}}. \end{aligned} \quad (\text{A20})$$

In words, the Multiple Event Statistic for a possible detection is divided by the square-root of the reduced chi-square for each of the chi-square statistics computed above, resulting in two discriminators.

B. Ephemeris-Matching Calculation Used in KOI-TCE Comparisons

Consider a TCE which is characterized by its period T_{TCE} , epoch t_{TCE} , and trial transit pulse duration D ; on the same target star, consider a KOI which is characterized by its

period T_{KOI} and epoch t_{KOI} . The following calculation can be used to determine whether the two ephemerides represent a good match or a poor match in transit timing.

First, of the two periods, define T_{short} to be the shorter, and t_{short} to be the corresponding epoch (i.e., if the KOI has a shorter period, then $T_{\text{short}} \equiv T_{\text{KOI}}$ and $t_{\text{short}} \equiv t_{\text{KOI}}$); define T_{long} and t_{long} to be the period and epoch of the ephemeris with the longer period. The ephemeris matching parameter is the fraction of transits predicted by $(T_{\text{short}}, t_{\text{short}})$ which fall within $D/2$ of one of the transits predicted by $(T_{\text{long}}, t_{\text{long}})$.

The reason for using the fraction of short-period transits which are predicted is that there will always be more short-period transits than long-period ones. In the case of an extremely large mismatch in periods between the two ephemerii (for example, a 3 day and a 300 day period), it is possible for all of the longer-period transits to fall close to transits of the shorter period, but the reverse is not true. Thus, in cases of extreme mismatch in period, using the fraction of short-period transits as the metric ensures that matching parameter has a low value, whereas the fraction of long-period transits which fall near a short-period transit can be large, and thus use of the long-period transits in this way could result in a large value of the matching parameter even though the ephemerii are wildly mismatched.

The duration of the trial transit pulse must be included because the finite pulse width and the finite duration of a real transit result in a family of nearly-degenerate (period,epoch) combinations. For example, a dataset which contains 3 transits of 13 hour duration at 365 day period would be well-matched by a model transit with 365 day period, but almost equally well by a transit with 364.9 day period or 365.1 day period. The matching parameter takes this degeneracy into account by requiring that the short-period transits be within one-half of a trial transit duration of the long-period transits. The duration “smearing” is applied to the longer-period ephemeris because, in a case with a huge period mismatch, applying it to the short-period ephemeris could result in duty-cycle problems. For example, consider the match between a 365 day period ephemeris with 13 hour duration and a 1 day period ephemeris. Applying the pulse duration smearing to the short-period ephemeris would result in a duty cycle greater than 0.5; applying the smearing to the long-period ephemeris ensures that such absurd combinations of parameters do not occur.

REFERENCES

- Allen, B. 2004, Phys. Rev. D 71, 062001
- Borucki, W.J., et al. 2010, ApJ, 713, L126
- Caldwell, D.A. et al. 2012, ApJ 713, L92

- Christiansen, J.L. et al. 2012, arXiv:1208.0595
- Gilliland, R.L. et al. 2011, ApJS197, 6
- Haas, M.R. et al.2010, arXiv:1001.0437
- Jenkins, J. M. 2002, ApJ, 575, 493
- Jenkins, J.M. et al.2010, arXiv:1001.0258
- Jenkins, J.M., et al. 2010, Proc SPIE 7740,77400D
- Seader, S., et al. 2012, in preparation.
- Smith, J.C. et al. 2012, PASP124, 1000.
- Stumpe, M.C. et al. 2012,
- Tenenbaum, P. et al. 2012, ApJS199, 24
- Twicken, J.D., et al. 2010b, Proc SPIE 7740, 77401U
- Wu, H. et al. 2010, Proc SPIE 7740, 774019

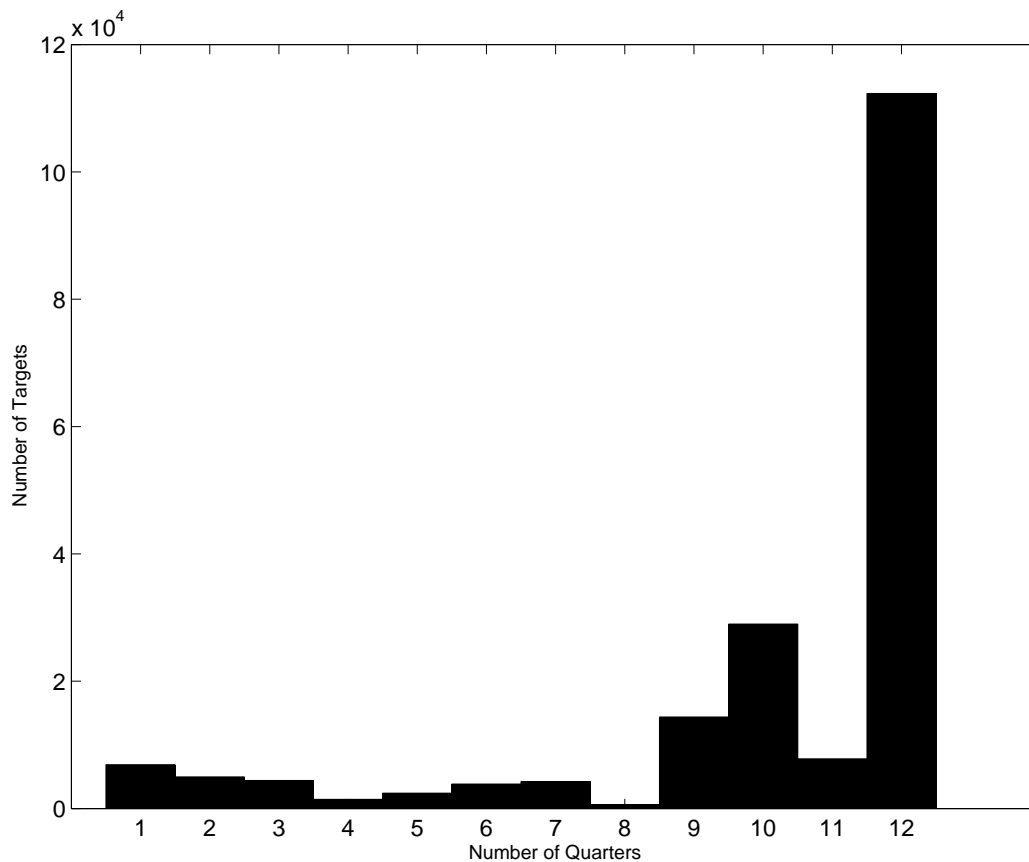


Fig. 1.— Histogram of number of quarters of observation for all targets. The significant number of targets observed for 10 quarters out of 12 is primarily due to an onboard electronics failure which prevents readout from 4 out of the 84 CCD modules on the focal plane, resulting in a “blind spot” which rotates through the field of view as *Kepler* rotates about its axis.

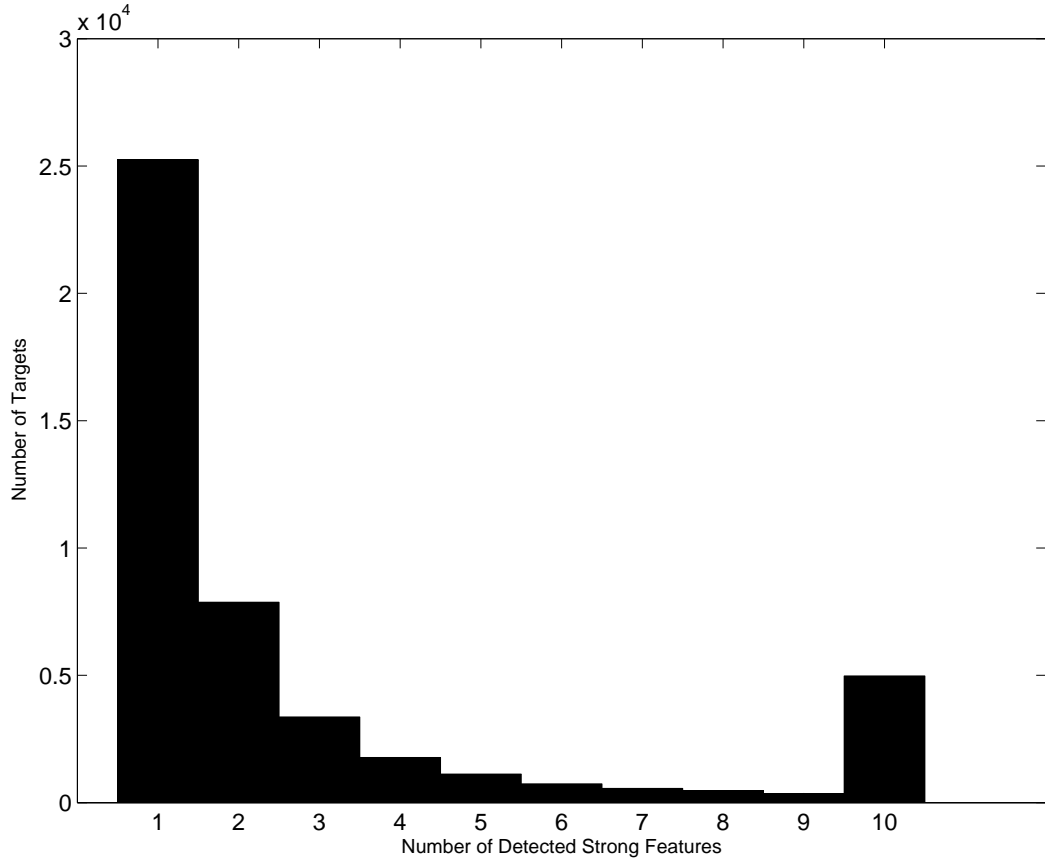


Fig. 2.— Distribution of the number of strong features in each flux time series, as defined in the text. The final bin includes overflows: there are a total of 327 targets with 10 features and 4,650 with more than 10 features.

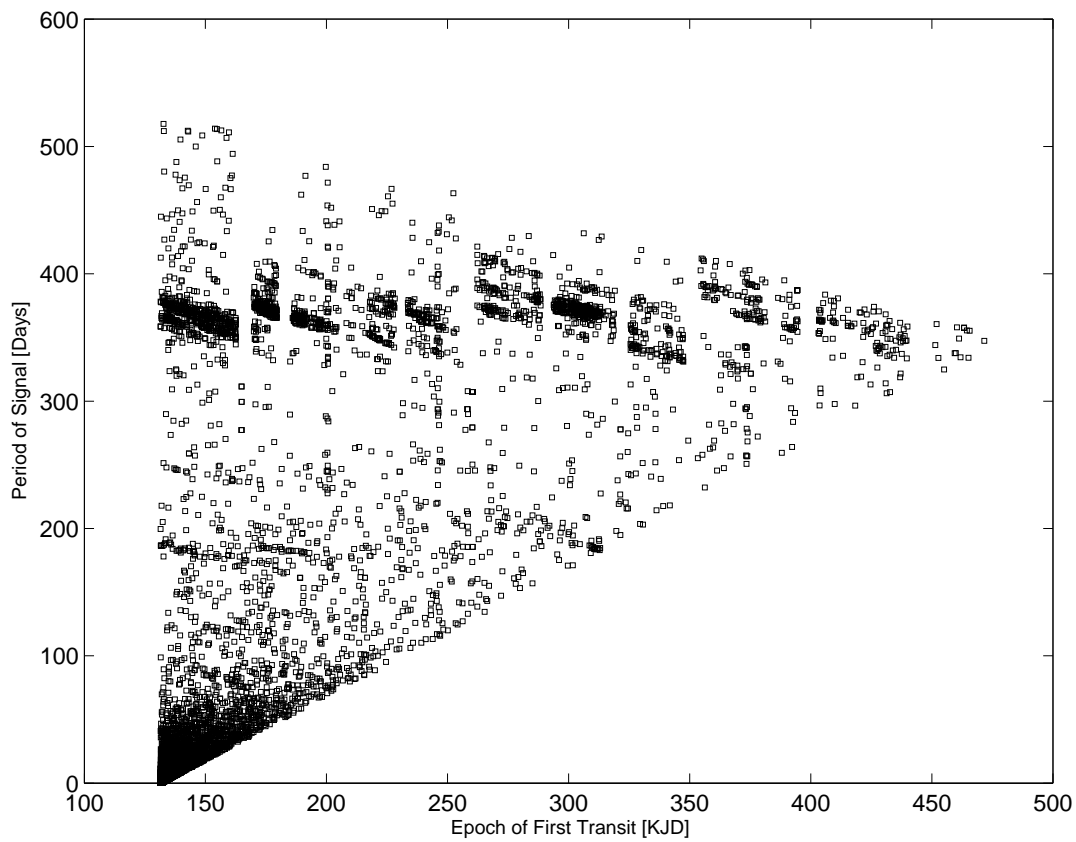


Fig. 3.— Epoch and period of the 18,427 TCEs detected in the 12-quarter TPS run. Periods are in days, epochs are in Kepler-modified Julian Date (KJD), see text for definition.

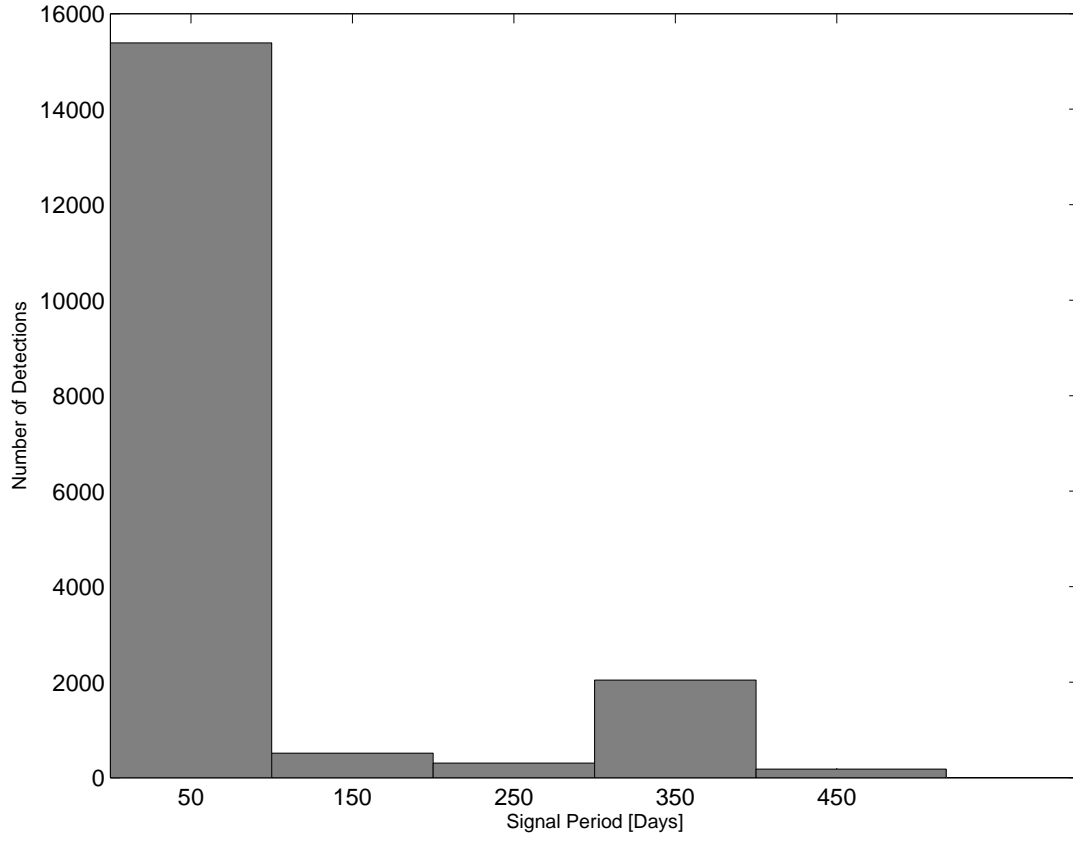


Fig. 4.— Distribution of TCE periods. The excess of detections at periods close to 1 year is due to the rotation of a small number of image artifact channels about the focal plane as *Kepler* rotates about its axis.

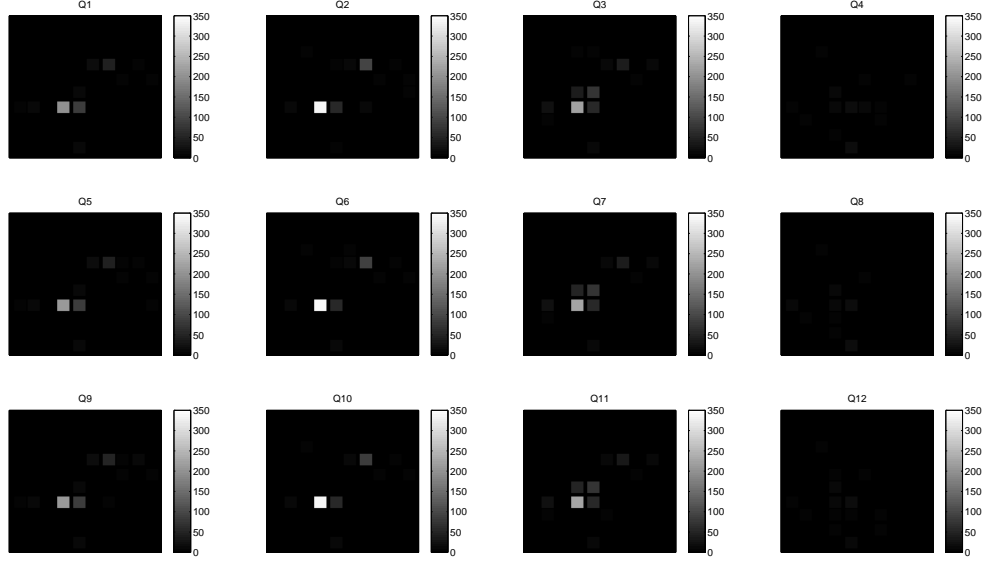


Fig. 5.— Participation of *Kepler* output channels in TCEs with periods between 300 and 400 days. The sub-plots are all oriented such that modules 2, 3, and 4 are at the top. The strongest contributions come from Module 17, Output 2, which is known to exhibit temperature-dependent noise artifacts. Other strong contributors shown are Module 9, output 2; Module 13, Output 4; and Module 18, Output 2. All of these channels are also known to exhibit unusually elevated noise, though not at the level of Module 17, Output 2.

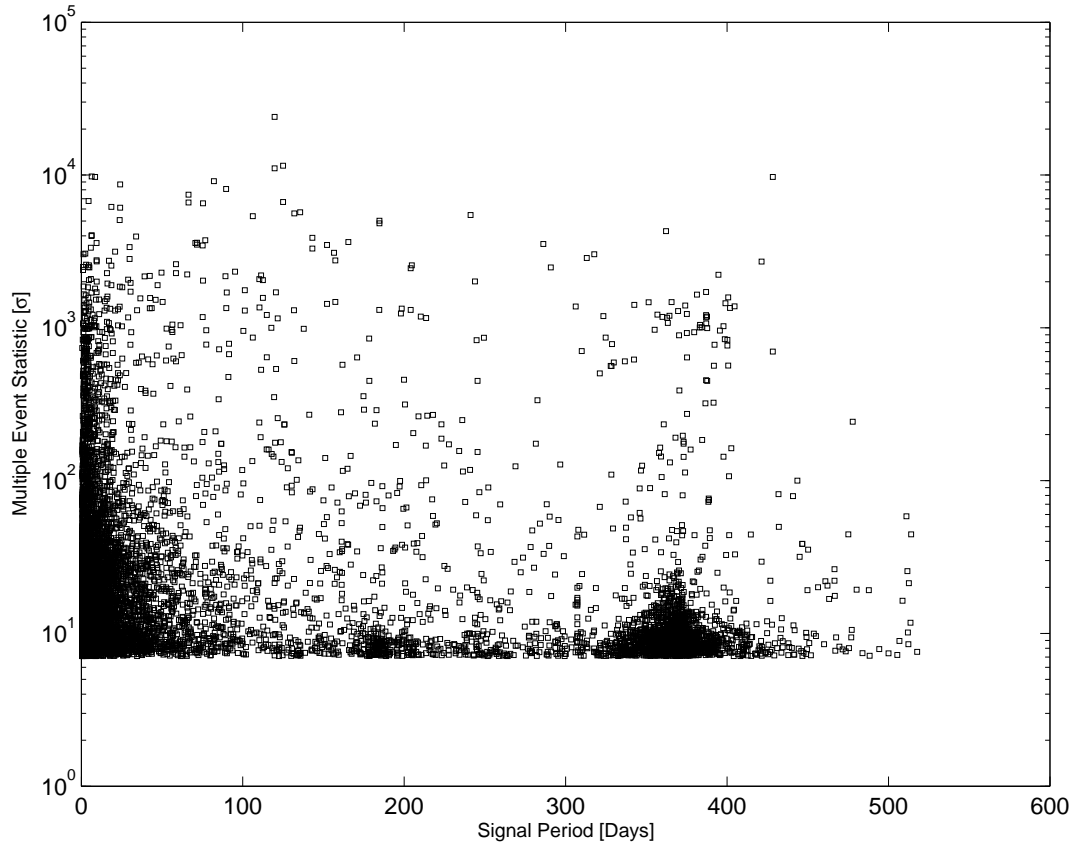


Fig. 6.— Distribution of TCE periods and Multiple Event Statistics.

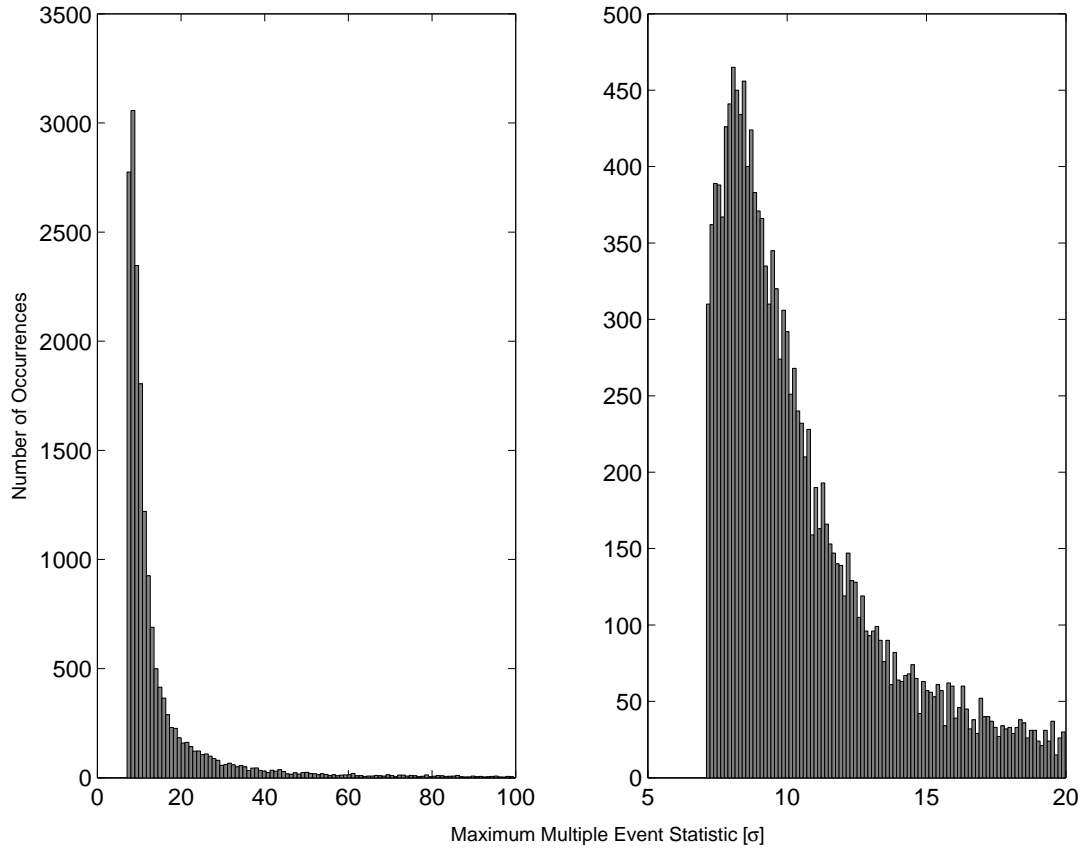


Fig. 7.— Distribution of Multiple Event Statistics. Left: 17,568 TCEs with Multiple Event Statistic of 100 or lower. Right: 15,018 TCEs with Multiple Event Statistic of 20 or lower.

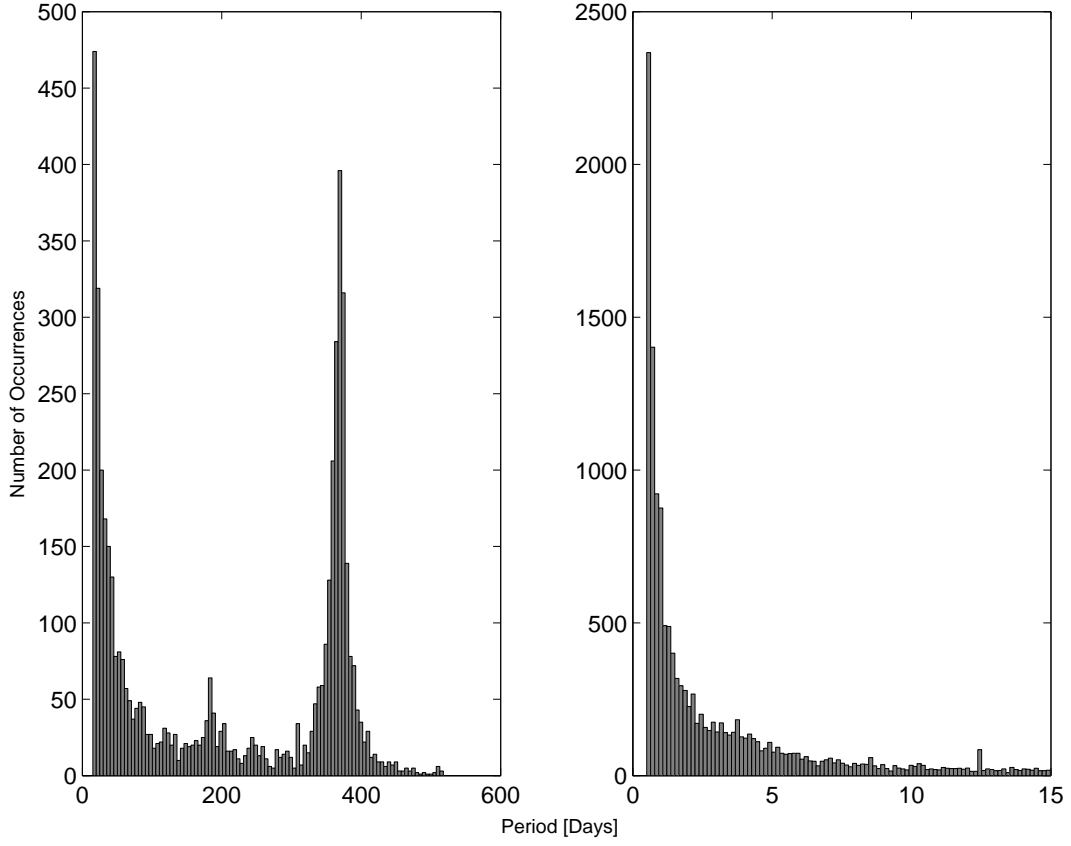


Fig. 8.— Distribution of periods. Left: 5,045 TCEs with periods greater than 15 days, with the data anomaly-driven excess at approximately 1 year clearly visible. Right: 13,382 TCEs with periods less than 15 days.

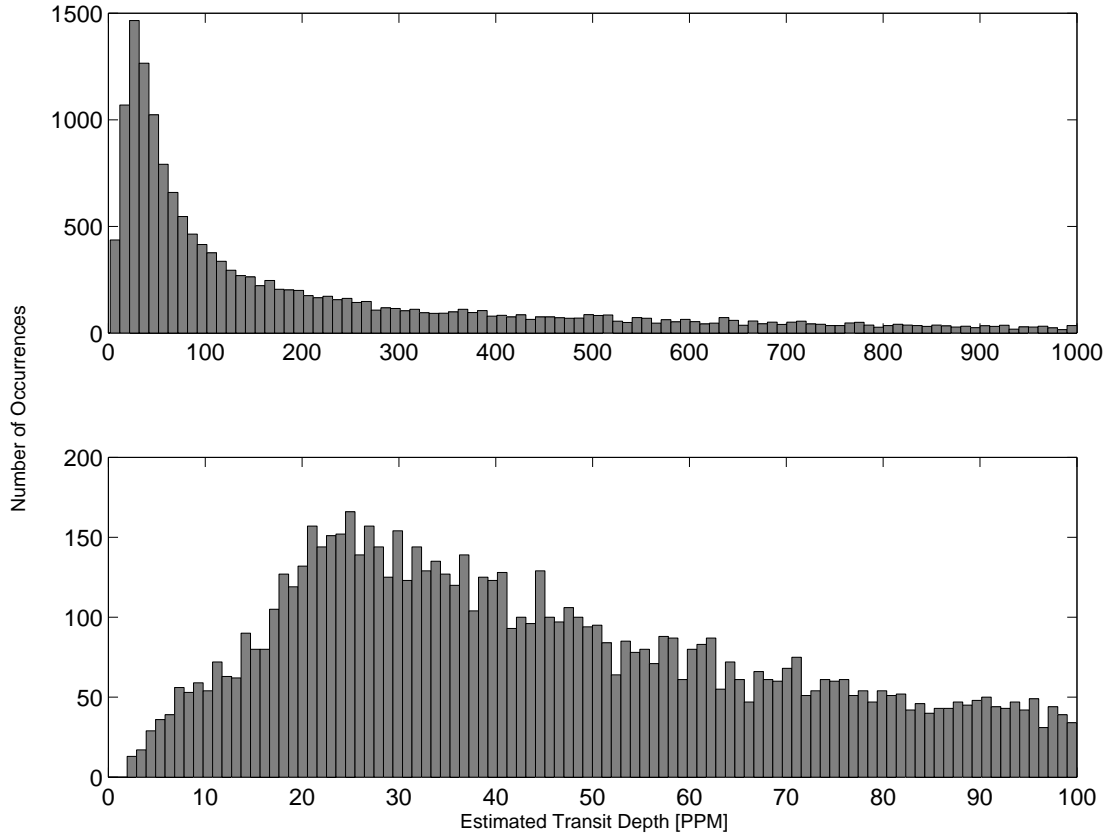


Fig. 9.— Distribution of estimated transit depths. Top: 16,115 signals with estimated depth of 1,000 parts per million (PPM) or less; bottom: 8,068 signals with 100 PPM or less.

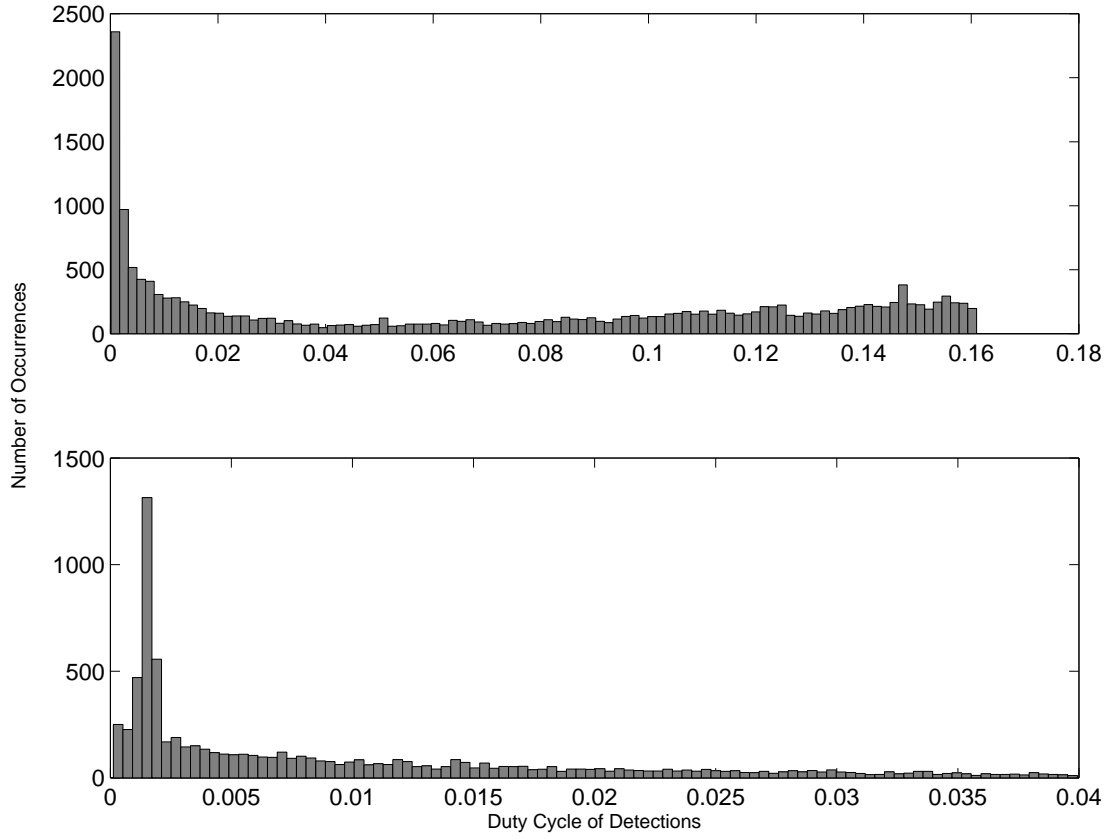


Fig. 10.— Distribution of transit duty cycles. Top: all TCEs. Bottom: 7,729 TCEs with transit duty cycle below 0.04.

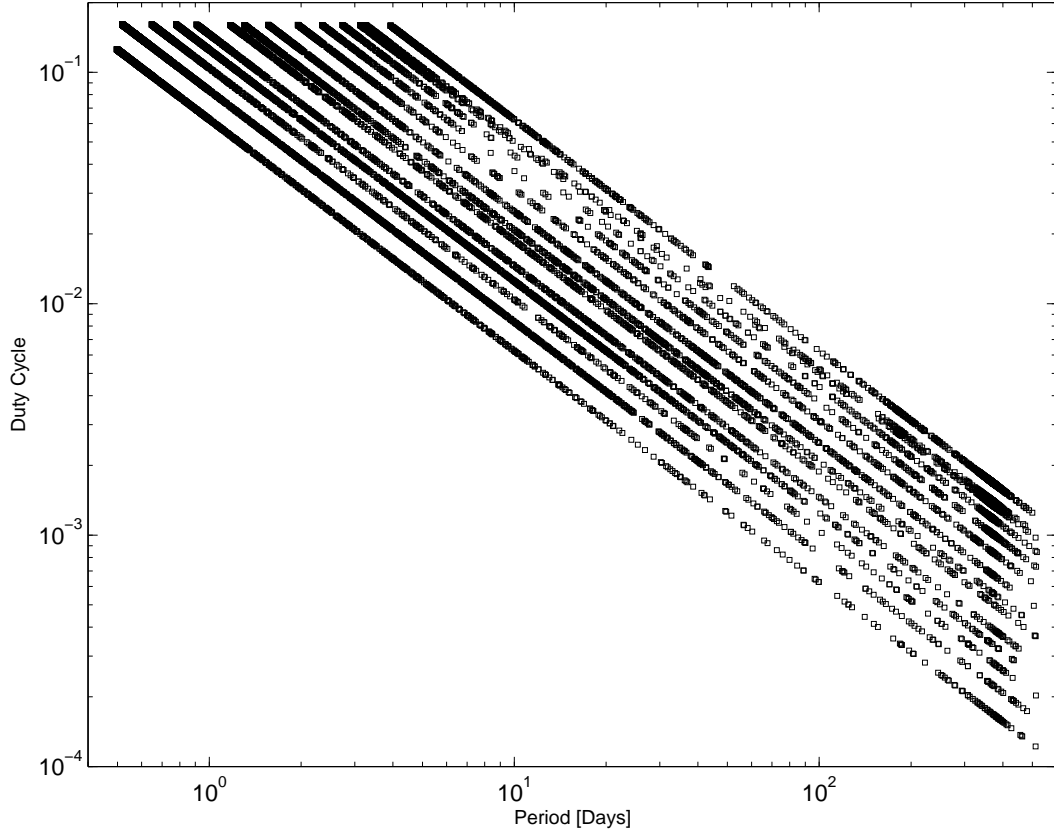


Fig. 11.— Relationship between period and transit duty cycle for all TCEs. The structure observed is driven by the fact that TPS uses a small number of fixed trial transit pulse durations for its searches, and by the fact that at a given trial transit pulse duration the transit duty cycle is inversely proportional to the TCE period.

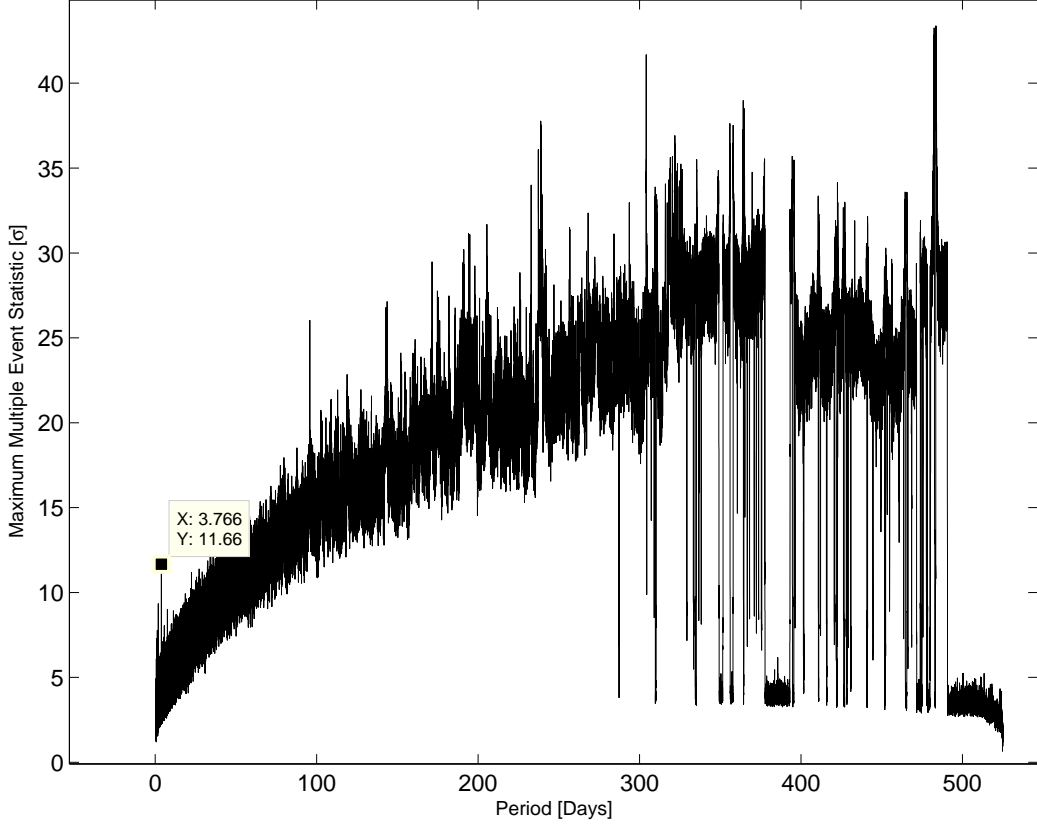


Fig. 12.— Maximum Multiple Event Statistic as a function of period for a sample target. In this target, the KOI period of 3.766 days is shown at the marker, with a Multiple Event Statistic of 11.66 σ . One or more artifacts in the flux time series are causing the large number of larger Multiple Event Statistic values at longer periods. Because of the 1,000 iteration limit on rejecting strong signals and re-searching for better but weaker signals, this KOI is not detected: the 1,000 iterations are exhausted before all of the false alarms in the figure can be rejected.

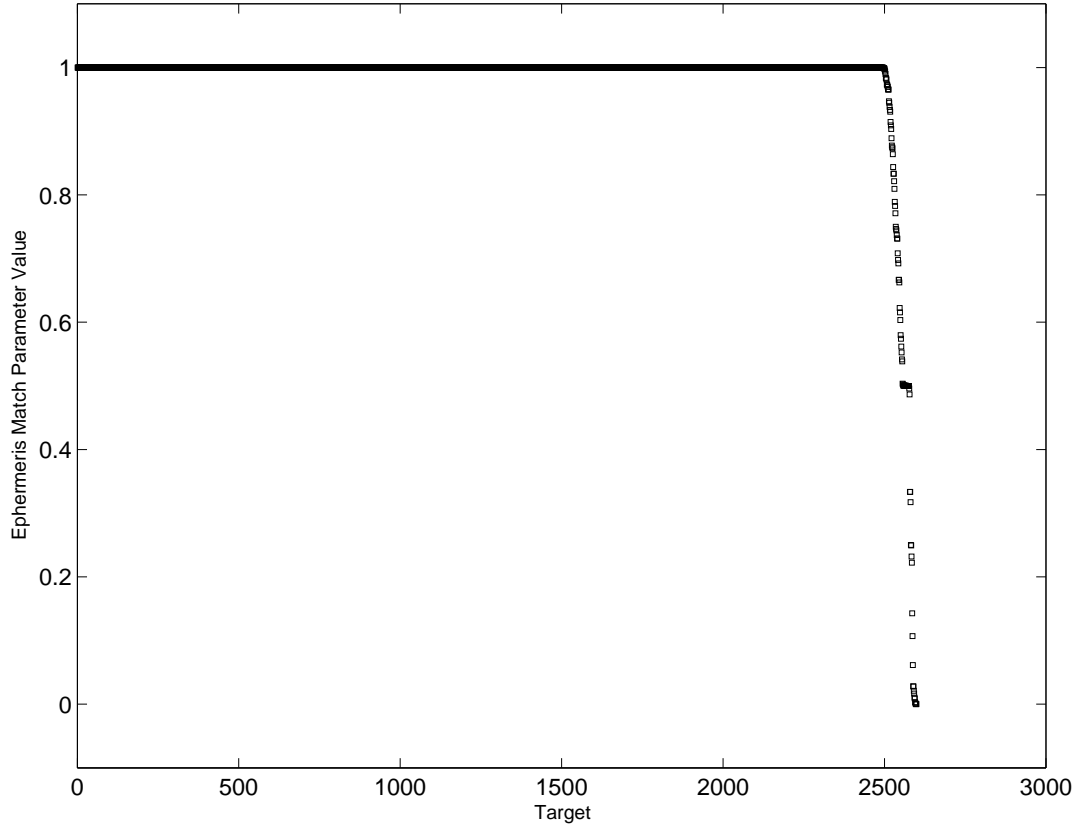


Fig. 13.— Value of the ephemeris-match parameter described in the text across all 2,608 TCEs which are matched to known KOIs. Only 113 of the values are not identically equal to 1.

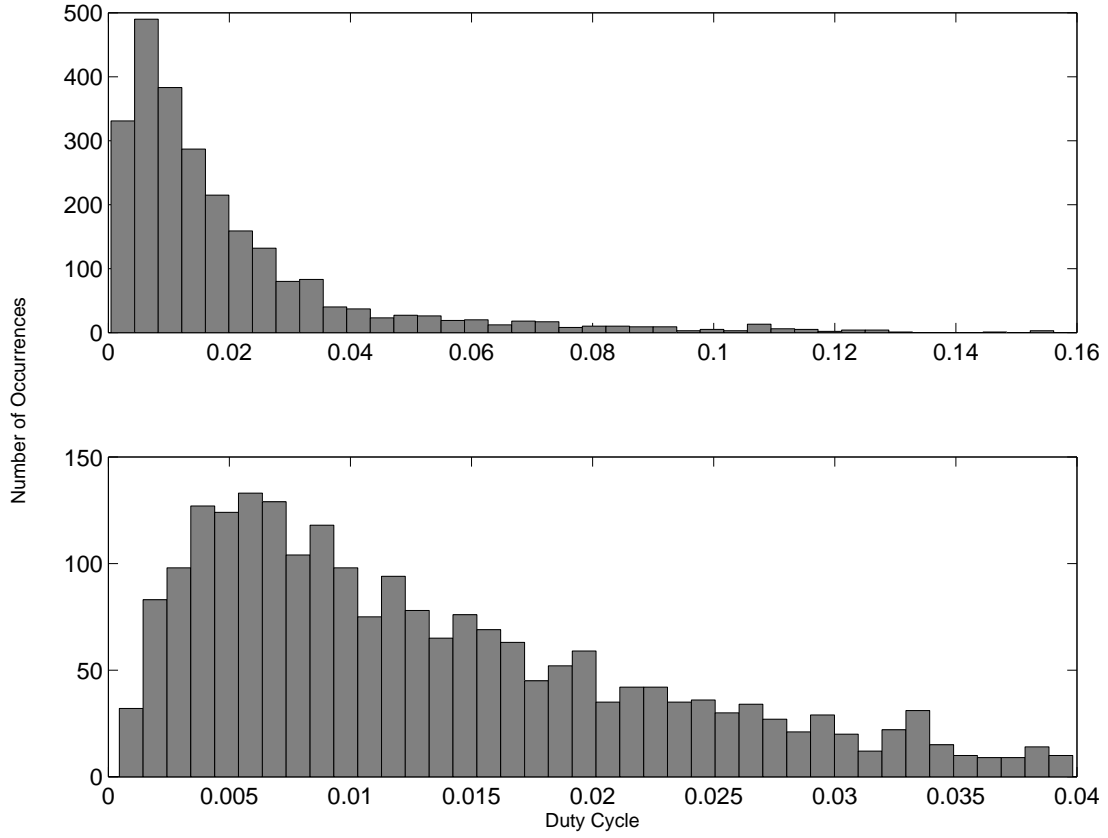


Fig. 14.— Distribution of transit duty cycles for TCEs successfully matched with KOIs. Top: 2,495 cases in which the ephemeris match is identically equal to 1. Bottom: 2,205 cases in which the ephemeris match is identically equal to 1 and the transit duty cycle is less than 0.04.

